Prediction of Maximum Lift Effects on Realistic High-Lift-Commercial-Aircraft-Configurations within the European project EUROLIFT II

H. Frhr. v. Geyr [1] and N. Schade [2],
German Aerospace Center (DLR), Lilienthalplatz 7, 38108 Braunschweig, Germany

Within the framework of the European project EUROLIFT II extensive numerical polar computations for three different stages of gradually increased geometrical complexity of the KH3Y aircraft configuration have been conducted. These challenging computations were performed through the complementary work of five different European institutions. The main objectives of these activities are the assessment of the capabilities of CFD to predict the dependence of the high-lift performance on the Reynolds number and to further improve the understanding of the high-lift associated vortex phenomena, especially the nacelle strake mechanism. The paper will present the key results and the main achievements, as obtained through the challenging research work assigned to Subtask 2.1.3 of the EUROLIFT II project. The focus will be put on the discussion on the aerodynamic phenomena underlined by the comparison of prediction and wind tunnel measurements.

Nomenclature

α	=	Angle of attack in degrees
Cp	=	Pressure coefficient
c_{fx}	=	Component of the projected skin friction tensor in the x direction
C_L	=	Lift coefficient
C_D	=	Drag coefficient
Ma	=	Mach number
Re	=	Reynolds number
μ_t	=	Turbulent dynamic viscosity

I. Introduction

The three-element high-lift system of commercial transport aircraft (slat, main wing and Fowler-type of flap) is well established with a very efficient compromise between the gain of lift and the complexity of the mechanical system. In principle the interaction mechanisms between the three elements are understood[1]. However, the geometry of realistic high-lift systems is more complicated and the interaction mechanisms are disturbed by vortex flows. The appearance of vortices is geometrically conditioned. Such vortices are generated by the sharp edges and affect the high-lift flow behavior of the configuration. For instance, the aerodynamic requirement of a clean transition of the wing leading edge to the fuselage at cruise conditions on one side and the deflection of the slat at high-lift conditions lead to the geometrical consequence of an onglet. When the slat is extended, parts of this onglet form a slat horn. The underwing engine installation leads to an even more complex situation. The deflection of the slat is interrupted at the position of the pylon, adding vortices to the flow field generated by the flanges of the slat cut-out. This slat

[1] Research Scientist, Institute of Aerodynamics and Flow Technology, Department of Transport Aircraft, heiko.vgeyr@dlr.de
[2] Research Scientist, Institute of Aerodynamics and Flow Technology, Department of Transport Aircraft,

cut-out in region of the engine and the presence of the engine lead to a significant loss of maximum lift compared to the high-lift configuration without engine. In order to recover these lift losses at least partially, strakes may be place on the nacelle. A strake is a geometrically small device which generates a strong distinct vortex. Placing this strake in a proper way on the nacelle a significant amount of the lift losses can be recovered.

Within the European project EUROLIFT II one of the main goals is the improvement of the understanding of the vortex developments and interactions associated with the high-lift flow field at maximum lift. To be able to study these phenomena systematically the complexity level of the EUROLIFT (I) KH3Y configuration is gradually increased in two steps towards a realistic configuration of modern commercial transport aircraft. The Stage 1 configuration represents the base high-lift configuration and is equipped with an onglet and slat horn only, i.e. the engine installation is neglected. In the next stage, designated as Stage 2, a Through-Flow-Nacelle is installed representing a modern high-bypass ratio engine. In the final Stage 3 configuration a nacelle strake is added. In Figure 1 all three configurations are shown with the geometrical differences marked in color.

Within EUROLIFT II comprehensive wind tunnel measurements in the Low Speed Wind Tunnel (LSWT) of Airbus Germany as well as in the European Transonic Wind tunnel (ETW) in Cologne, Germany, have been conducted for all three stages at Reynolds number ranging from $Re=1.3\cdot10^6$ up to $Re=25\cdot10^6$. The results of these measurements serve as a comprehensive database which is used to validate the numerical methods.

The numerical computation of the high-lift flow for such configurations especially at maximum lift conditions is still very challenging and not a standard procedure. Within the Subtask 2.1.3 of EUROLIFT II five partners (Airbus-France, Alenia Aeronautica, DLR, FOI and NLR) took this challenge and conducted numerical polar computations for all three configurations at three different Reynolds numbers applying the European state-of-the-art Reynolds Averaged Navier Stokes (RANS) solvers. The key objectives of this work are to assess the capabilities of CFD to capture maximum lift, to capture the Reynolds-number dependence of maximum lift and to analyze the vortex phenomena associated with the high-lift flows of the different configurations in order to improve the understanding of the dominant effects. Of special interest are the associated stall mechanisms and the strake effect.

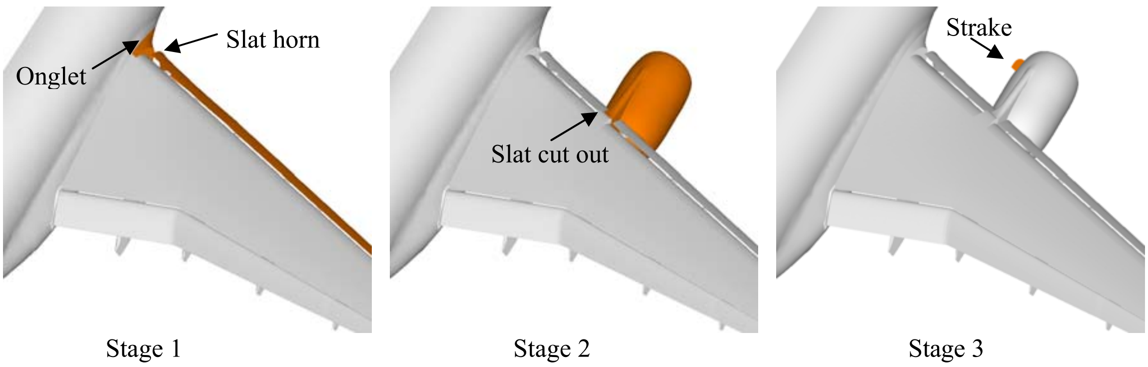

Figure 1. Extension stages of the KH3Y-configuration towards a realistic high-lift aircraft configuration.

II. Grid generation and test case matrix

Within the Task 1[2] activities of the EUROLIFT II project it has been shown that even small geometrical details such as the slat tracks of the wind tunnel model have a non-negligible influence on the lift behavior and the reachable level of maximum lift. Therefore the already high geometrical complexity of the Stage 1 to Stage 3 configurations is further extended by including the slat tracks as well as the pressure tube bundles between the slat and main wing which connect the pressure holes in the slat with the transducers. These bundles are places aside each slat track as illustrated in Figure 2.

The Stage 1, Stage 2 and, Stage 3 configurations have been generated based on the geometry description of the KH3Y landing configuration using CATIA V5[3]. Based on the water-tight surface description of each stage different grid generation systems are applied. DLR, NLR, FOI and Alenia (ALA) applied RANS-solvers based on unstructured methods. In order to minimize the grid dependence of results obtained by those partners computing the same test case, common unstructured grids were generated. The grid generation challenge of these complex configurations was taken by Airbus-France (A-F) as an opportunity to assess the capabilities of the Chimera technique following the structured grid approach. Table 1 gives an overview of the different grid generation systems applied, the solvers used and the test cases which are computed by each partner.

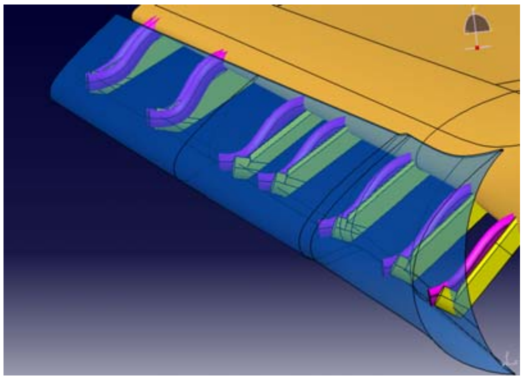

Figure 2. Slat tracks and pressure tube bundles included in the CFD-geometry description.

			LSWT			ETW					
			Re=1.33·10^6			Re=15·10^6			Re=25·10^6		
		Stage	1	2	3	1	2	3	1	2	3
Partner	Grid Generation	Test Case / Solver	401	404	407	422	442	462	442	444	464
DLR	Centaur[4]	TAU[6]	✓	✓	✓	✓	✓	✓	✓	✓	✓
NLR	FASTFLO[5]	FASTFLO-TAU[6]		✓			✓			✓	
FOI	-	EDGE[7]				✓	✓		✓	✓	
Alenia	in-house software[16]	UNS3D[8]				✓			✓		
A-F	ICEM HEXA[10]	elsA[9]				✓			✓*		

Table 1. Methods used and test cases computed by each partner (* simplified geometry).

In order to allow computations on common grids the grid size had to be limited. Therefore the following simplifications had to be applied:

- *The flow is treated as fully turbulent for all Reynolds numbers*: Complete transition data for the full range of the polars and for all above listed test cases are not available from experiments or can be predicted within the required accuracy for such complex configurations.

- *Deformation is not considered*: Deformation is unimportant for the LSWT test cases and from the Task 1.1 activities it is concluded[2], that deformation has only a secondary effect on maximum lift for the Reynolds number of Re=15·10^6. Including deformation would require closed coupled CFD-FEM computations for each angle of attack but such an approach is beyond the scope of the Subtask 2.1.3 activities.

- *Free-flight computations:* The investigations of model installations, conducted in Task 1.1, clearly indicate that the effects on the lift and drag behavior as well as on maximum lift are not negligible. But in-tunnel computations are beyond the scope of this subtask activities.

DLR generated common grids for the LSWT test cases using the Centaur software package4. By the placement of different sources and the use of anisotropic stretching the grid resolution of the surface as well as in the grid domain has been adjusted aiming to achieve high resolution with a minimum amount of grid nodes. The same objective holds for the grid generation by NLR applying the FASTFLO system5. NLR generated the common grids for the ETW test cases where one grid per configuration is designed to serve both Reynolds-numbers. Both partners followed the same strategy to minimize the differences in the quality of the grids for all three stages: The starting point marks the Stage 3 configuration as it is the most complex one and thus requires the most sources. Especially the capture and trace of the vortex of the nacelle strake requires a very high local grid resolution sufficient to capture the vortex through the range of angles of attack. The trajectory of the vortex, i.e. its path through the domain, was determined through an initial computation of different angles of attack.

The grid for the Stage 2 configuration is obtained by retaining all sources of the Stage 3 grid and replacing only the surface panel of the nacelle at which the strake is attached. This approach is followed by DLR and ensures that the re-meshing of the configuration leads to a grid of the same quality as the Stage 3 one. A slightly different approach is followed by NLR. Here the surface mesh is locally modified and a complete re-meshing of the configuration is avoided. The Figure 3 shows exemplary the resulting surface grids of the Stage 3 configurations by DLR and NLR. Both partners used 30 prismatic layers and a height of the final prismatic layer which covers the boundary layer height. For the LSWT test cases a total grid size of 18·106 nodes and for the ETW test cases a grid size of 14·106 nodes in total was obtained. Alenia applied their in-house grid generation method16 which allows anisotropic stretching ratios of up to 30. The geometry does not consider the slat tracks and the pressure tube bundles. By the use of 14 prismatic layers Alenia produced a hybrid grid for the Stage 1 of the size of 830.000 nodes in total.

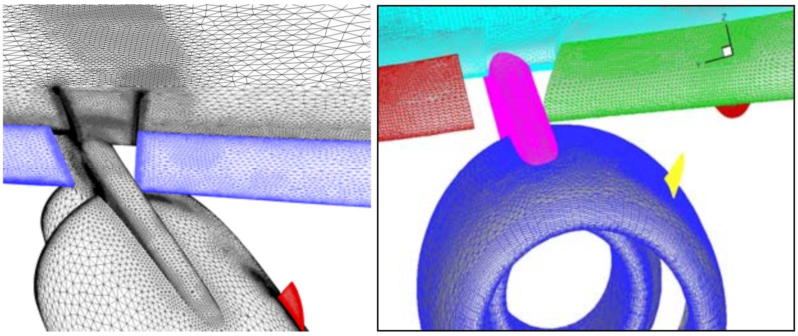

(a) (b)

Figure 3. Exemplary surface grids of (a) DLR and (b) NLR

The Chimera approach followed by Airbus-France uses ICEM HEXA[10] for grid generation and leads to a grid of the size of $22 \cdot 10^6$ nodes with 111 blocks in total. Due to unresolved problems in the interpolation between the background grid and some Chimera blocks the Stage 1 configuration had to be simplified. The slat tracks, pressure tube bundles and 4 of the 5 flap track fairing were not considered. The following figure 4 depicts the obtained surface grids of Alenia and Airbus-France.

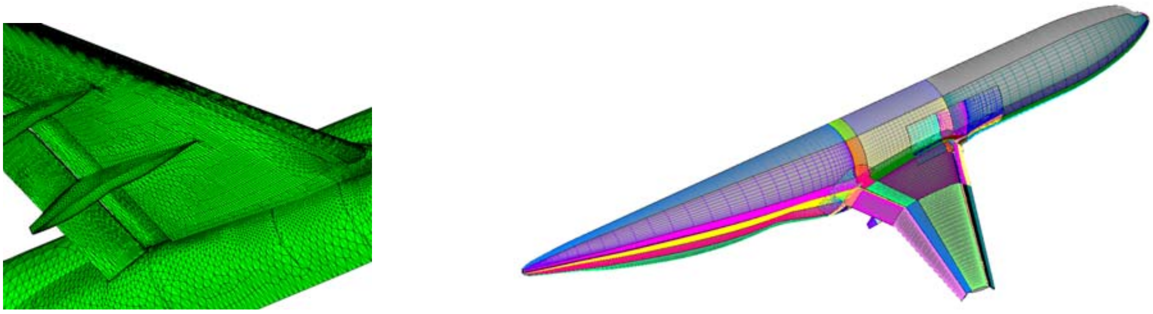

(a) (b)

Figure 4. Exemplary surface grids of (a) Alenia and (b) Airbus-France

III. High-lift performance and maximum lift prediction

A. Low Reynolds-number test cases (LSWT)

The first presented results are the computations of the LSWT-test cases TC401, T404, and TC407. These test cases correspond to a free-stream Mach number M=0.176 and a Reynolds number of $Re=1.33 \cdot 10^6$. All Cp-distributions which will be presented are taken in the cross sections DV1, DV6 and DV10. The location of these pressure lines are depicted in Figure 5. Figure 6 shows exemplary the comparison of the predicted and measured Cp-distributions of the Stage 2 configuration at $\alpha=12.35°$ in DV1 and DV10. The predictions of DLR and NLR correspond well to the measured Cp-distribution in DV10. The small deviations between the two numerical results at the slat are due to a slight difference in the orientation of the slat cutting plane used to extract the Cp-distribution. At DV1 less agreement between experimental and numerical results is obtained. Differences are observed among both numerical results as well. These differences are surprising, because both partners use the same CFD-code, the same solver settings, the same turbulence model, and compute on identical grids. A detailed investigation shows that this discrepancy is attributed to a different number of flow solver iterations. Based on experience gathered in the EUROLIFT I project with low Reynolds number high-lift computations NLR has taken 3000 multi-grid cycles. DLR has taken 15000 multigrid cycles. At a first glance the lift and drag coefficients appear to be converged after 3000 multigrid cycles. However, by taking more flow solver iterations lift decreases with approximately 10 lift counts. The differences between the DLR and NLR result indicates that the inboard flow separation very slowly develops.

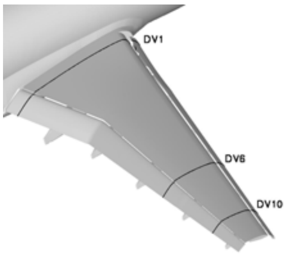

Figure 5. Location of Cp-measurement cross sections

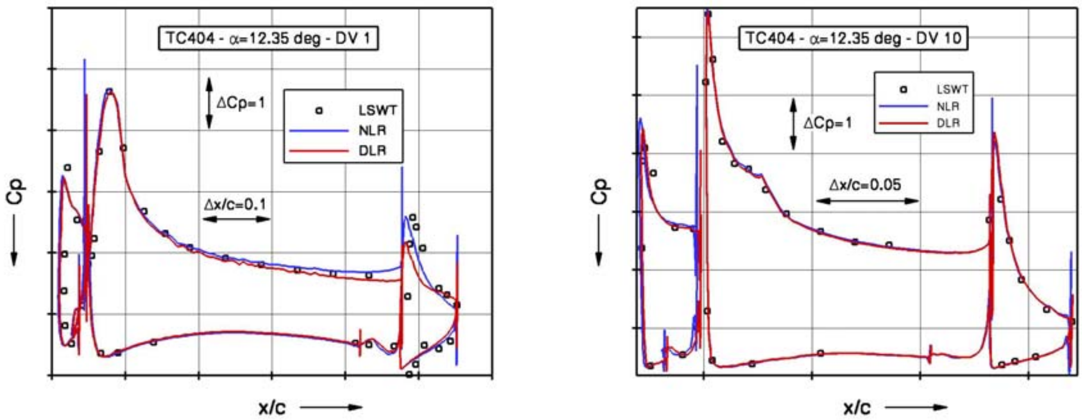

Figure 6. Comparison of Cp-distribution of two partners cross plotted with the LSWT measurements for Stage 2 for α=12.25° at DV1 and DV10.

Figure 7 shows the skin friction lines for this test case for both computations. Both results are very similar except that DLR predicts larger sized regions of flow separation. These regions are indicated by the red colored c_{fx}-values in the DLR result. Considering the significant differences in the used number of iterations it is concluded, that the boundary layer on all three high-lift elements takes much longer to completely develop through the transient phase of the convergence compared to the boundary layer at transonic free-stream conditions. The difficulty in high-lift flow is the interdependence of the boundary layer of all three elements. Analysis of the convergence behavior underlines that depending on the angle of attack the global coefficients appear converged as they retain at an almost

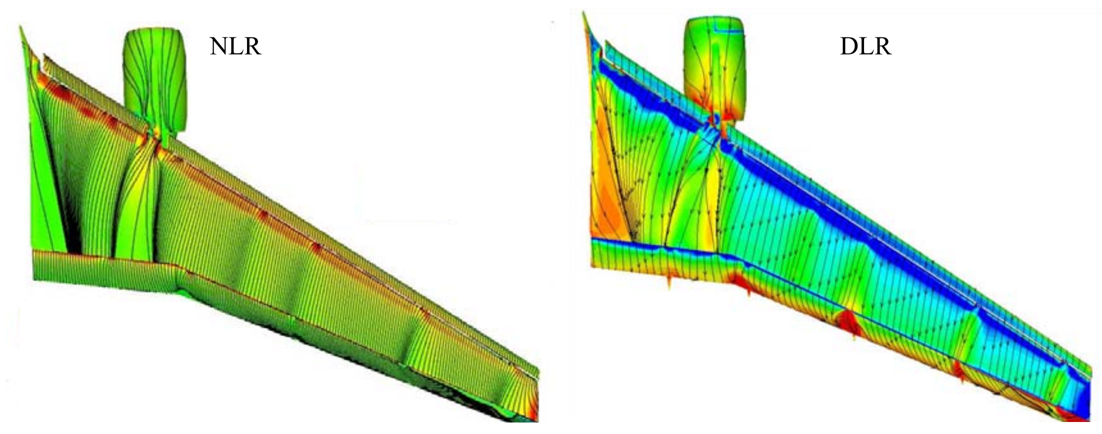

Figure 7. Comparison of the skin friction lines: NLR Cp-colored; DLR c_{fx}-colored

constant value for several hundreds of iterations. Continuing the computations can lead to a sudden decrease as the flow separations develop or extend is size.

The reason for the observed deviations between the measured and predicted Cp-distribution in DV1 is found in the analysis of the peniche and wind tunnel wall effects as performed in the Task 1.1 activities. Such model installation effects induce spanwise cross-flow velocities which lead to an increased inboard loading[14,2]. As the numerical computations are performed in a free-flight set-up, the inboard loading has to be lower as in the half-model measurements. Therefore the DV1 measured Cp-values should be slightly lower especially at the slat compared to the numerical results.

However, through the application of suitable wind tunnel correction methods the lift curve and polar should be corrected for these installation effects. In Figure 8 the computed and measured lift curves as well as the polars of all three stages are cross plotted. The dashed lines denote the measurements and the solid lines are assigned to the numerical results. For all three stages the lift seems to be under-predicted in the linear range of the lift curve. Maximum lift on the other hand is predicted within an accuracy of 1.5%. The highest lift and lowest drag are measured for the Stage 1 configuration which also predicted by CFD. With the engine installation a significant loss of maximum lift and an increase in drag are measured. This influence of the engine installation on the global coefficients is captured by the numerical results. As the nacelle strake is added, approximately 60 to 70% of the loss in maximum lift is recovered, which is again very well predicted by CFD. Adding the strake is not producing any noticeable drag increase according to the measurements which is consistently predicted by CFD.

It is therefore concluded, that CFD is capable to predict the effect of geometrical changes (Stage 1 to Stage 3) within a good accuracy. However, the direct comparison of the measured and predicted values shows non-negligible differences. The computations seem to under-predict the measured lift coefficient for a given angle of attack and to over-predict drag. According to Reference[11] transition has an only minor effect of the lift curve. Model deformation effects can be neglected due to the atmospheric test conditions and the stiffness of the wind tunnel model. The main reason is considered to be the model installation effects as analyzed in the Task 1.1 activities. Additionally, the numerical results itself contain non-physical, spurious drag components which to some extend contribute to the over-prediction of drag. This drag component will be further analyzed for the ETW test cases and discussed in this context.

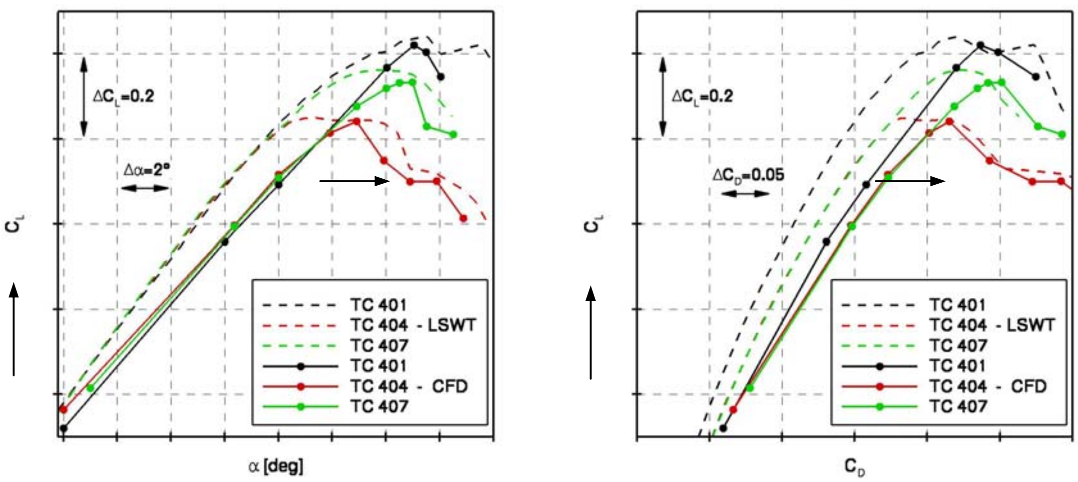

Lift curves Lilienthal polars

Figure 8. Comparison computed and measured lift curves and polars for all three Stages.

Figure 9 depicts the computed skin friction lines for the Stage 3 configuration in comparison to flow visualization results obtained during the LSWT tests for the same test case. All main flow features and effects as visible through the skin friction lines are captured by CFD. From this result and the discussed lift behavior it can be concluded that the CFD is well capable to predict the strake effect within good accuracy. The accuracy in predicting the influence of such geometrical differences on the changes of maximum lift underlines further the validity of the applied grid generation strategy.

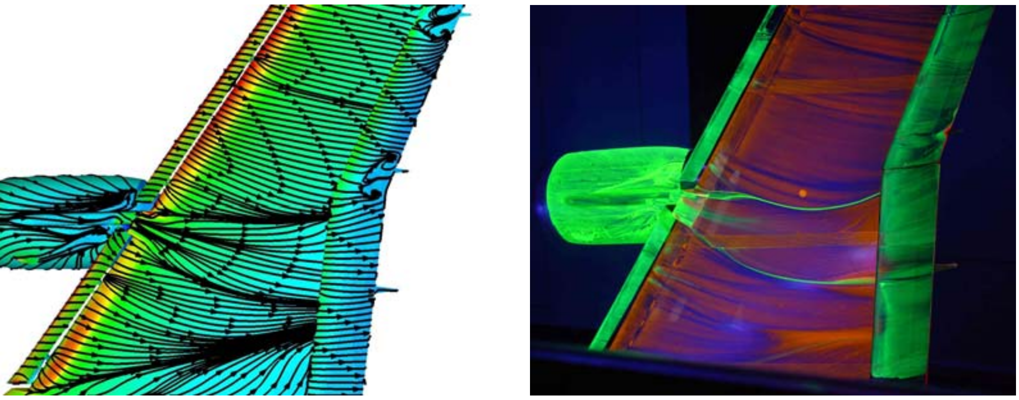

Figure 9. Limiting streamlines at α=18.5°, Stage 3.

B. High Reynolds-number test cases (ETW)

Most partners concentrated on the ETW-test cases of the Stage 1 configuration (TC422 and TC424). FOI and DLR computed on the common hybrid grids generated by NLR applying different turbulence models. FOI exclusively used the k-ω EARSM turbulence model by Hellsten[14] whereas DLR applied the one-equation Spalart-Allmaras model with the Edwards[12] modification. Alenia computed on own grids using the same turbulence model as FOI. But it has to be considered, that the slat tracks and pressure tube bundles are not considered in the geometry description of Alenia. Apart from the unstructured methods Airbus-France applied the Chimera approach using a structured method. Structured grids appear to be less dissipative than grids based on tetrahedral elements which would make the comparison of these results with the results of the unstructured methods very interesting. Unfortunately shows the applied Chimera approach difficulties in some regions of the configuration to find valid interpolation coefficients necessary for the data exchange from the back-ground grid to the Chimera block and vice versa. Due to the occurrence of so called orphan points the complexity of the geometry was reduced in terms of neglecting the slat tracks, pressure tube bundles and flap track fairings. Figure 10 shows the obtained lift curves for $Re=15\cdot10^6$ and $Re=25\cdot10^6$ in comparison to the ETW-measurements. Lift is under-predicted in the region of maximum lift where as a match of the measured data seems to be obtained in the linear range of the lift curve. However, the measured trend of maximum lift increase from $Re=15\cdot10^6$ to $Re=25\cdot10^6$ is well captured. The good match of the computed and measured lift curve in the linear range has to be put into perspective to the circumstance of the missing geometrical details. A final assessment of their effect on the lift curve and maximum lift using the structured approach could not be made. However, the analysis of these effects by applying unstructured methods (Ref. 2) indeed shows a non-negligible decrease of lift.

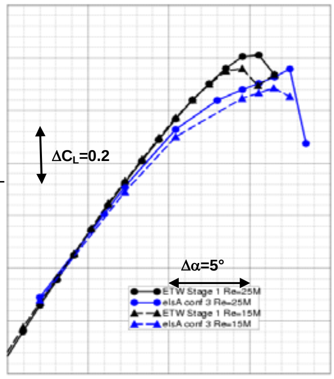

Figure 10. Results for simplified Stage 1 geometry (structured approach)

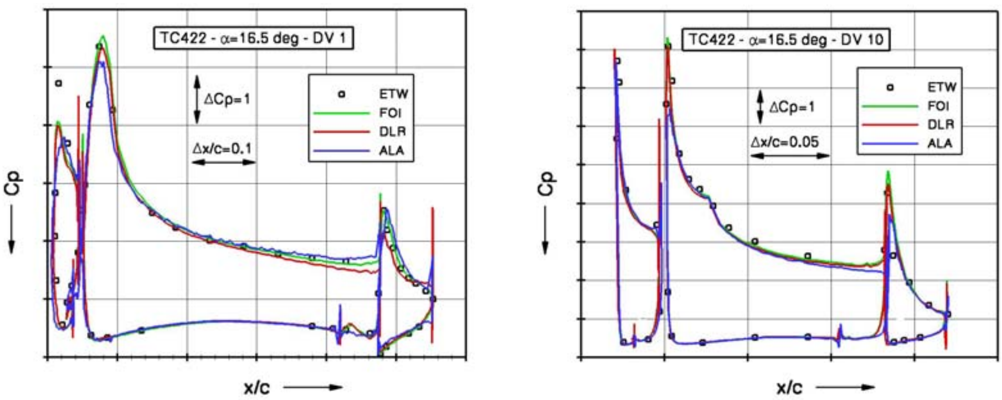

Figure 11. Comparison of Cp-distributions for TC422.

Putting the focus now on the results of the unstructured methods, Figure 11 shows a comparison of the predicted Cp-distributions of DLR, FOI, and Alenia for the Stage 1 configuration at α=16.5° exemplary for Re=15·106. The measurements are cross-plotted and marked with symbols. For all computations a good agreement with the measured data is obtained in both cross-sections. The visible deviations of the measured and computed Cp-distributions of the slat in DV1 are attributed to the half-model effect as outlined in section A. The main differences between the computational results occur at the suction peaks on all three high-lift elements. FOI computes higher suctions peaks on all elements leading to the visible difference of the pressure level on the trailing edge of the main wing. In contrast to FOI pre-conditioning is applied by DLR which reduces the numerical dissipation level and usually leads to increased suction peaks compared to results of a non-pre-conditioned computation. Hence, the observed deviations between DLR and FOI results are considered to be mainly caused by the different turbulence models.

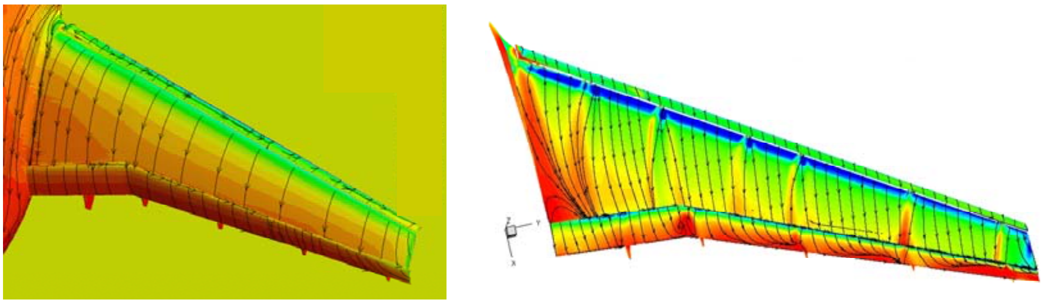

Alenia DLR

Figure 12. TC424: Skin friction lines at α=19°.

The results of Alenia show the lowest suction peaks in both cross sections. Especially at DV1 the lowest pressure level on the main wing and the flap are computed by Alenia in spite of the under-prediction of the suction peaks. Similar results are obtained for the TC424 which underlines, that the observed differences in the numerical results are Reynolds-number independent. The DV1-cross section (see Figure 5) is located very close the wing root. Here the flow behavior is dominated by the interaction of the boundary layers of the fuselage and the main wing leading to the forming of the horse-shoe vortex and its separation from the main wing trailing edge. The skin friction lines, depicted in Figure 12 for Alenia and DLR results, do not show the expected outboard bending in the wing root section in case of Alenia. Results without slat tracks and pressure tube bundles obtained within the Task 1.1 activities show an outboard bending of the skin friction lines. Thus, the outboard bending of the skin friction lines in case of the DLR result is not caused by the slat tracks and bundles. The reason for the differences can not be pin-pointed. The most likely explanation is the resolution of the grid in normal direction of the fuselage surface in the wing root region. As visible in Figure 4 Alenia applied here a high cell stretching in spanwise direction whereas the common grid has been refined in this region. Additionally Alenia uses half of the number of prismatic layers as has available in the common grid.

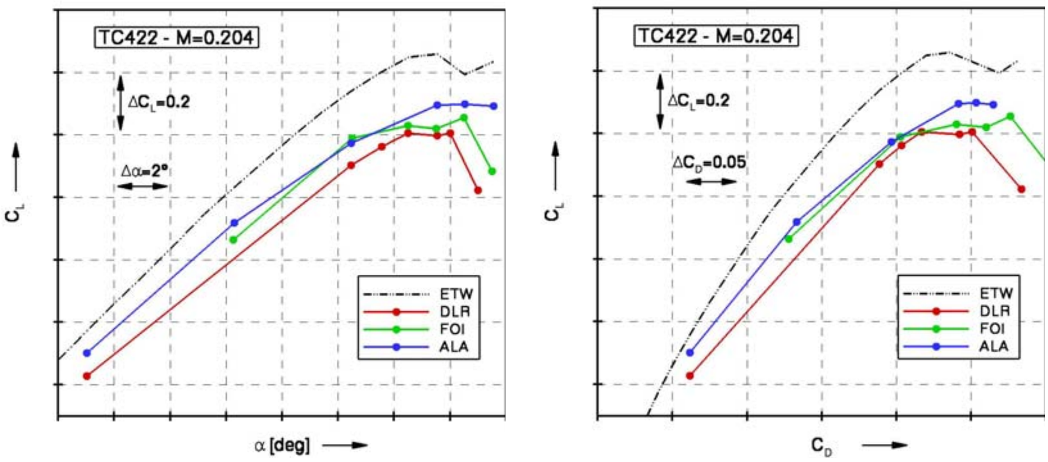

Figure 13. Computed lift curves and polars in comparison with the measurements for TC422.

The obtained lift curves and polars are depicted in Figure 13 for the Stage 1 configuration, cross plotted with the corresponding wind tunnel measurements marked with dashed lines. All numerical results under-predict lift and over-predict drag. In contrast to the LSWT-cases maximum lift is significantly under-predicted. The highest lift is obtained by Alenia, basically due to the lack of the lift reducing effect of the slat tracks and pressure tube bundles. DLR obtains the lowest lift and highest drag values which is consistent with the fact, that the size of the separation regions is predicted largest by DLR. Since the main difference is the applied turbulence model, it is concluded that the k-ω EARSM model as implemented by FOI leads to a lift prediction closer to the measurements. However, the influence of the turbulence model and the influence of the slat tracks and bundles are too small to close the gap to the measured lift and drag values. Figure 14 shows the comparison of the computed and measured lift curves and polars for TC442. Again the maximum lift is under-predicted and drag is over-predicted. Differences occur between the lift curves predicted by DLR and NLR. The same trend has been found earlier by comparing the LSWT results of both partners.

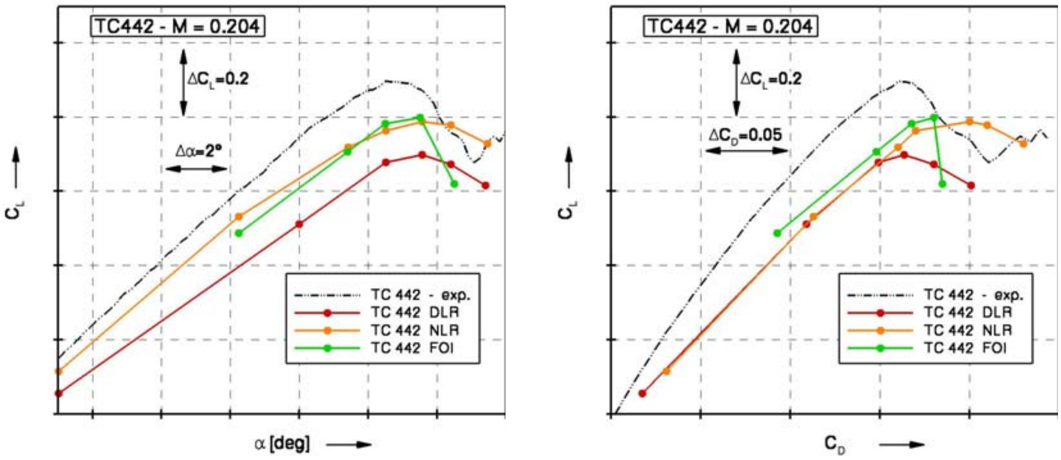

Figure 14. Computed lift curves and polars in comparison with the measurements for TC442.

The significant deviation between the numerical results and the measurements in terms of lift and drag can be only partly explained by the influence of the numerical method or applied turbulence model. The analysis of the model installation at ETW conditions, performed for the take-off configuration, show (Reference 14) a non-negligible effect on the lift curve and maximum lift. However, these effects can not fully close the gap to the measurements. In connection with the results of Alenia the problem of a proper grid resolution has been indicated. Even though, all generated grids have been produced according to the best practices available at that time, the main influence on the numerical results is seen in the grid.

In order to provide an insight into the grid dependence of the results, ONERA has performed far-field drag analysis for the DLR, NLR, and the FOI results of TC444 at α=16.5° based on the methods outlined in Reference 15. The method allows the determination of the physical drag components by identifying and isolating the non-physical, spurious drag. The conventional near-field drag determination by performing the integration of the pressure and skin friction distribution across the wetted surface leads to results which are contaminated by the spurious drag. Thus, near-field drag evaluation leads to a drag level higher than the physical drag. For a correct determination of the viscous shear layer and hence the viscous drag, a correct threshold of the ratio of the eddy viscosity to the molecular viscosity is important. Figure 15 shows the differences in the level of the eddy viscosity exemplary for the FOI and the DLR results. These differences are directly attributed to the applied turbulence model and stress the necessity to use different threshold values depending on the used turbulence model. For this test case the far-field drag breakdown reduces the near-field drag

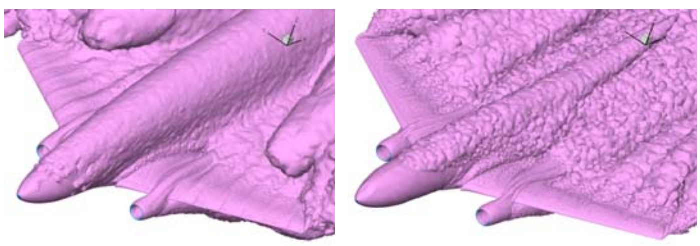

FOI: $\mu_t / \mu = 10.0$ DLR: $\mu_t / \mu = 1.0$

Figure 15. Different levels of eddy viscosity production depending on the turbulence model used for TC442 at α=16.5°.

by 1.65% for DLR, 0.6% for FOI and 2% for NLR. Facing the obtained deviation from the experimental drag values as shown in Figure 15 it can be stated, that the spurious drag influence is too small in order to be the only explanation. Additional far-field drag analysis performed by NLR leads to the same conclusion

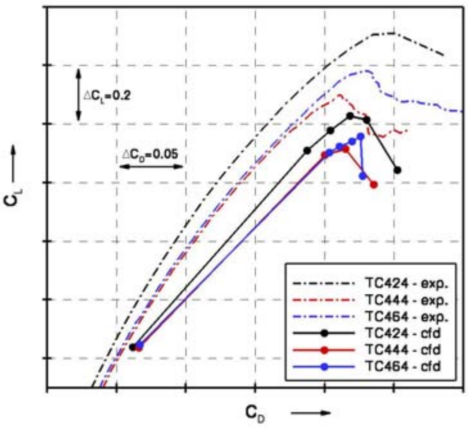

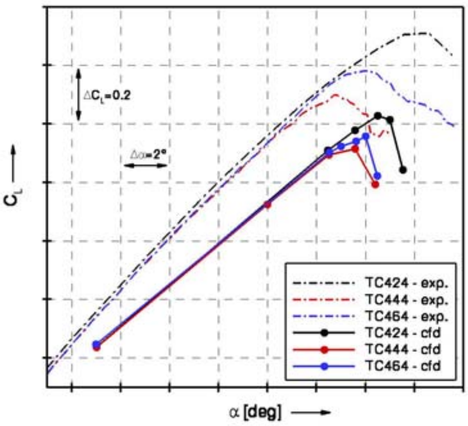

Figure 16. Computed lift curves and polars compared with measurements for all stages at Re=25·10^6.

All the above presented analysis of the differences in the partners' results aims to gain knowledge of the sensitiveness of maximum lift prediction to numerical and geometrical parameters. It has so far been shown that the prediction of absolute values is a challenging task for high-Reynolds number conditions. Figure 16 now depicts the CFD-capabilities to predict the impact of geometrical changes on the lift curve, the associated polars, and maximum lift exemplary for the Re=25·10^6. The Stage 1 configuration (TC424) shows the maximum lift and lowest drag. After engine integration a significant loss of maximum lift is measured. Minor influence is found in the linear part of the lift curve. Adding the installation drag shifts the polar to higher drag values. Different from the LSWT-measurements a very small drag increase is noticeable when the strake is added. This is due to the fact, that the strake itself and the strake position have been optimized at LSWT-conditions. The strake effect itself is less distinct at Re=25·10^6 than it is for the LSWT-conditions. At the highest Reynolds number only approximately 50% of the loss of maximum lift could be recovers in the experiments.

Putting the focus now on the computational results it is evident from Figure 16, that these geometrical effects as measured in the ETW-wind tunnel are well predicted by the CFD methods. The differences in maximum lift, the impact on drag and the maximum lift recovery are in a very good agreement to the measurements. A similar match of the measured geometrical effects are obtained for Re=15·10^6. Hence, it can be concluded that CFD is very well prepared and capable to predict the impact of geometrical differences within a good accuracy compared to measurements, whereas further effort is indeed necessary to be capable to predict the absolute values for a single configuration. However, it has to be stated, that an additional difficulty occurs for the computations at maximum lift. The lift breakdown is associated with the development of separations which grow in size as the angle of attack approaches α_{max} at which maximum lift is obtained. The flow is usually not fully steady, i.e. local unsteady flow features may occur. Therefore all presented values in the region of maximum lift are averaged values. The application of time accurate methods in this region could give a better indication of the unsteadiness of the flow, but such computations are beyond the scope of the activities.

Figure 17 shows the obtained bandwidth in maximum lift exemplary for the FOI results for the Stage 1 configuration. It can be seen that still a gap towards the measured values remains.

On the other hand a good agreement of the Reynolds-number dependence is obtained for the Stage 1 and the Stage 2 configurations. Even though the Reynolds number dependence is very small for the Stage 3 configuration an opposite trend to the measurements is shown. But the assessment for this configuration should reflect the sharp computed lift breakdown as depicted in Figure 17 whereas the measured lift breakdown appears to be softer. A smaller step size $\Delta\alpha$ in the region of maximum lift could lead to a further shift of maximum lift to a higher value and a larger angle of attack.

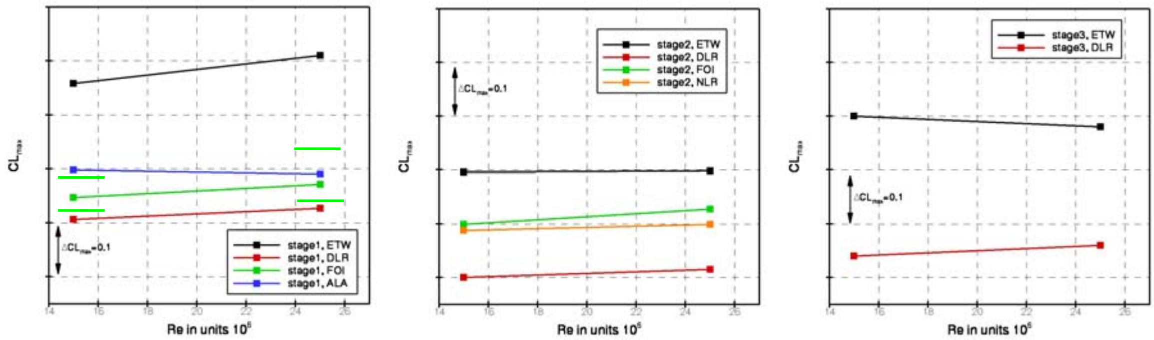

Stage 1 Stage 2 Stage 3

Figure 17. Computed and measured Reynolds-number dependence for the Stage 1, the Stage 2, and the Stage 3 configurations

The above presented results lead to the conclusion, that the applied CFD methods are very well capable to predict the Reynolds-number dependence even though there is room for further improvements. Especially the influence of deformation is an uncertainty at Re=25·106 which has to be address in a continuing future work.

IV. Prediction of stall mechanisms

The presented results of the global coefficients have shown so far that the CFD methods are capable to predict geometrical differences within a good accuracy. In the following the focus is put on more local effects aiming to assess the prediction capability of the stall mechanism. The wind tunnel measurements provide flow visualization results for selected test cases which serve as basis for the validation of the predicted stall mechanism.

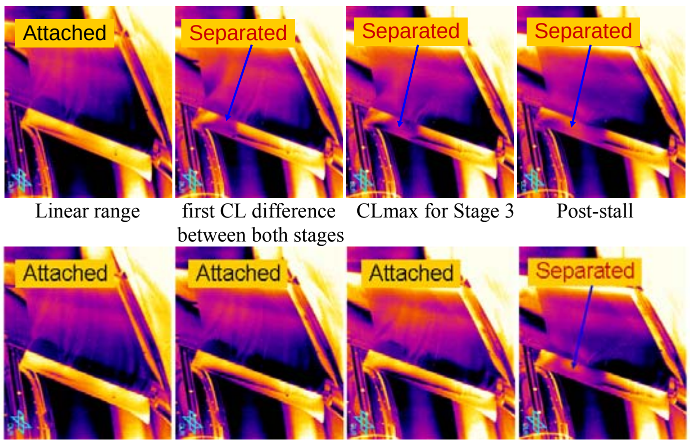

Figure 18. Infra-red pictures of the Stage 2 (top) and the Stage 3 (bottom) from pre-stall (left) to post-stall (right).

A. Stall mechanisms at LSWT-conditions

As exemplary results the stall mechanism of the Stage 2 and Stage 3 configurations will be presented, since the observed stall mechanism during the wind tunnel tests are very different. Figure 18 shows infra-red pictures of the Stage 2 (top) and the Stage 3 (bottom) at angles of attack from pre-stall to post-stall. As the angle of attack increases a separation develops close to the pylon of the inboard slat leading to a trailing edge separation of the main wing. This separation is not captured by the infra-red pictures since the object of interest has been the slat. As slat separation has developed, it retains for all higher angles of attack. When the strake is installed this slat separation is shifted into the post-stall region, hence to angles of attack beyond maximum lift. Thus the lift breakdown is not initiated by the slat stall as it is for the Stage 2 configuration.

Figure 19 depicts the predicted lift breakdown for both configurations. The contour-plot shows the c_{fx}-distribution where the red color denotes values below zero and hence separated flow. In agreement to the measurements of the Stage 2 configuration a flow separation on the inner slat close to the pylon is predicted prior to maximum lift. With the occurrence of this slat separation a trailing edge separation of the main wing develops. As the angle of attack increases further the trailing edge separation extends in spanwise direction.

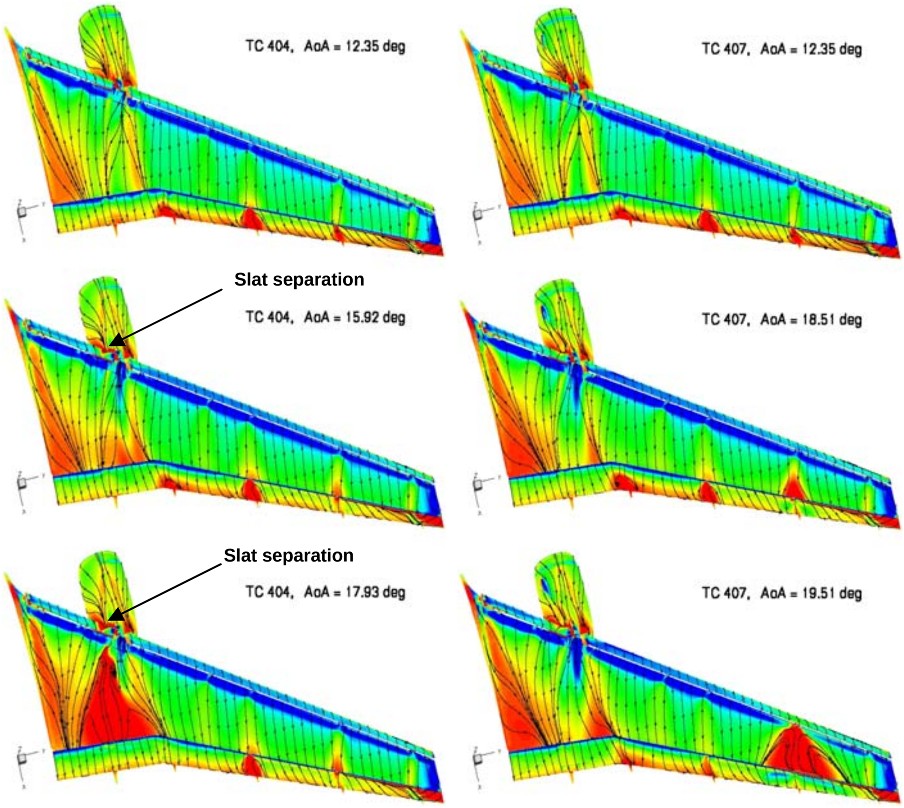

Figure 19. Predicted stall mechanism for Stage 2 (left) and Stage 3 (right).

The lift breakdown of the Stage 3 configuration is dominated by an outboard separation on the main wing at the spanwise position of the 6th slat track at which two pressure tube bundles, one on each side of the track, are installed. The inboard slat stays attached up to maximum lift. Hence, it is concluded, that the stall mechanisms for the low Reynolds-number cases are captured by CFD.

B. Stall mechanisms at high Reynolds numbers (ETW)

For both Reynolds numbers similar stall mechanisms occur. An indication of this similarity is found in the measured smooth transition from maximum lift to post-stall visible in the associated lift curves for both Reynolds-numbers. The most interesting stall mechanisms occur for the Stage 2 and the Stage 3 configurations which will be presented here for TC444 and TC464. For validation purpose a limited number of mini tufts pictures have been taken during the ETW-tests for selected number of test cases. In Figure 20 such a mini tuft picture is depicted for TC442 at α=16°, with the flow coming from the right. The fuselage is located close to the top. A slat separation is visible outboard of the inner slat and at the trailing edge of the main wing.

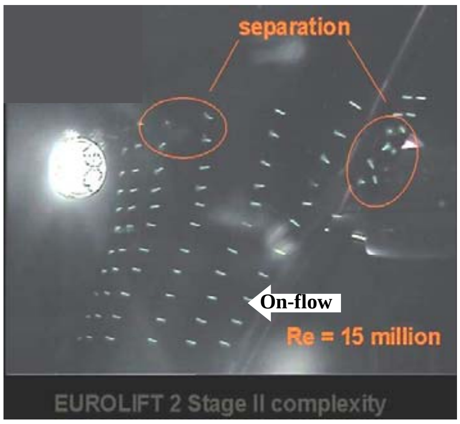

Figure 20. Mini tufts at α=16° for the TC442.

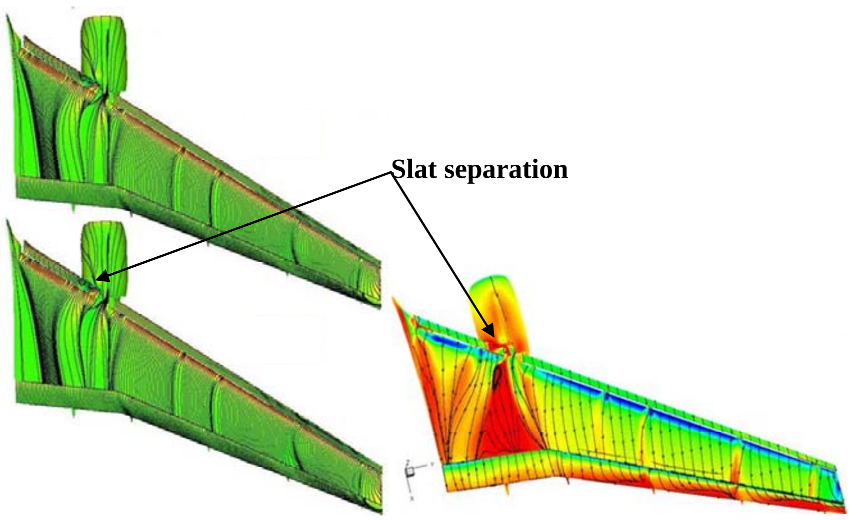

Figure 21. Predicted stall mechanism for Stage 2 from pre-stall (top) to maximum lift (bottom).

The same separations are predicted by CFD for Stage 2 as indicated by the skin friction lines, which are depicted in Figure 21. The left part of this figure shows the Cp-distribution on the surface predicted by NLR whereas the right part depicts the skin friction lines overlaid on the c_{fx}-distribution as a result of the DLR computation. Both skin friction distributions in the lower part of the figure are obtained for similar angles of attack which are very close to maximum lift. The differences in the numerical results are the effect of the different numbers of iterations used as outlined previously. Even though the sizes of the separation regions on the main wing differ, both computations predict a stall mechanism consistent to the wind tunnel measurements. Similar results are obtained for the prediction of the stall mechanism for the Stage 3 configuration. The slat separation is inhibited until the angle of attack of maximum lift is passed. The lift breakdown is here initiated by the growing of the wing root separation. In contrast to the LSWT conditions no outboard flow separation at the 6th slat track is obtained at high Reynolds number conditions. Therefore CFD is capable to predict the stall mechanisms for all configurations and Reynolds-numbers considered consistent to mechanisms identified in the wind tunnel tests.

Lift recovery by the nacelle strake has evidently been demonstrated in the wind tunnel test and it has been shown, that CFD is capable to predict this effect within good accuracy. The strake effect is outlined more detailed in Figure 22 showing a close up of the skin friction lines on the inner slat and the nacelle of the Stage 2 and the Stage 3 configurations. The contour plots denote the c_{fx}-distribution on each configuration, where the red color indicates negative c_{fx}-values and thus separations. The slat separation is clearly seen for the Stage 2 configuration. At the rear part of the inboard side of the Stage 2 nacelle the skin friction lines merge into a separation line. In this region a strong nacelle vortex is found which is visualized in Figure 24. The color denotes the strength of the x-vorticity component with the blue color indicating a counter-clockwise rotation. As the nacelle strake is added, this strong nacelle vortex has almost vanished. The blue color of the strake vortex indicates the same sense of rotation as the nacelle vortex. As can be seen from TC464 in Figure 23 some rotational flow in the region of the nacelle vortex of TC444 is visible but in a much weaker form due to the influence

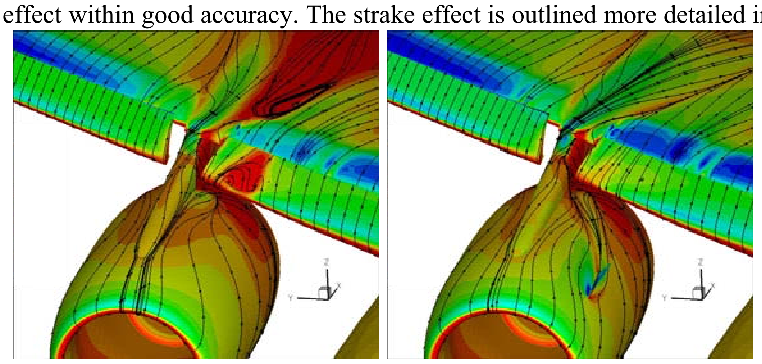

Figure 22. Effect of nacelle strake on flow topology for Re=$25 \cdot 10^6$ and α=17.5° (Stage 2 left; Stage 3 right picture).

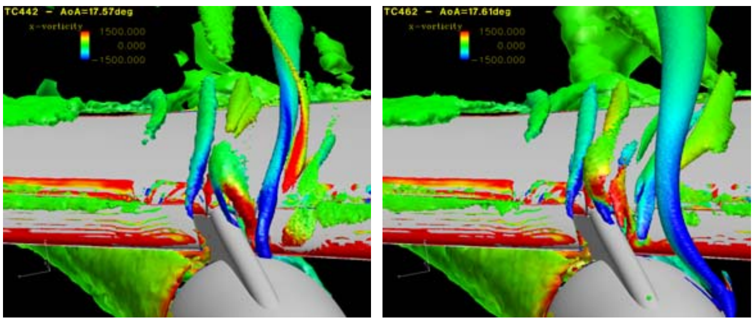

Figure 23. 3D vortex visualization.

of the strake vortex. The result of this change in the vortex structure is an attached flow on the slat as shown in Figure 23 for TC464.

V. Conclusion

The current paper summarizes the activities performed in Subtask 2.1.3 "Numerical Investigations" within the framework of the European project EUROLIFT II. Applying state-of-the-art RANS methods numerical computations for three different modifications of the KH3Y high-lift configuration have been performed by five partners. The objectives of the polar computations are the assessment of the CFD capabilities to capture maximum lift for different geometrical complex high-lift configurations, to capture the Reynolds-number dependence of maximum lift, and to improve the understanding for the vortex phenomena associated with the high-lift flows of the different configurations. Within the paper the obtained numerical results have been compared to wind tunnel measurements, conducted within EUROLIFT II for a range of Reynolds-numbers and for all three stages of the KH3Y configuration. From these comparisons the following conclusions are drawn with respect to the outlined objectives:

- The applied CFD methods are capable to predict the effect of geometrical details on the lift behaviour and maximum lift.
- The Reynolds-number influence is predicted in qualitative agreement to the wind tunnel measurements.
- The stall mechanisms are captured by CFD.
- The strake effect is predicted within good agreement to the measurements which underlines the validity of the applied grid generation strategy.
- Insights to strake mechanism are obtained by CFD leading to a further understanding of the vortex phenomena and interaction.
- Maximum lift is under-predicted for all configurations independent of the solver settings.
- Different grid generation strategies show a non-negligible effect on the computed lift which indicates a high sensitivity of the maximum lift on the grid resolution.
- Under-prediction of lift at ETW conditions seems to be too high in order to be fully explained by the lack of the installation effects:
  - → Future work necessary to identify best practise approach for high-lift grid generation
  - → Future work necessary to include installation effects by cost intensive in-tunnel computations
- The far-field drag analysis offers a big potential for grid quality assessment and physical drag determination,
  - → Future work is necessary to increase the level of reliability.

The presented results underline, that the current state of 3D high-lift performance prediction already reached a high level but room for further improvements have been identified. In a constitutive next step all the lessons learned with respect to transition, the geometrical effects, deformation, and half-model effects have to be combined in a final validation step, i.e. a final numerical prediction exercise in which all aspects are considered at the same time. This final validation would quantify the remaining uncertainties. Furthermore, the results presented indicate, that obtained results in maximum lift are sensitive to the grid resolution.

Finally, a lesson learned is that the computational effort for studying maximum lift behavior for a complete high-lift configuration is quite large. A sufficient number of flow solver iterations need to be taken to reach a solution of high accuracy. A challenge will be to introduce new algorithms to reduce this computational effort.

Acknowledgments

The research work discussed in this paper was performed within the European project EUROLIFT II (European High-Lift Programme II) as part of the 6th European Framework Programme, which is co-financed by the European Commission under the contract number AST-2004-502896.

The authors would like to thank Nicola Ceresola from Alenia Aeronautica S.p.A., Ronan Herry from Airbus France, J.W. v.d.Burg from National Aerospace Laboratory (NLR), P. Eliasson from the Swedish Defense Research Agency

(FOI) and S. Esquieu from Office National d'Etudes et de Recherches Aerospatiales (ONERA) as partners of this research activity.

This paper was originally presented on the 25th AIAA Applied Aerodynamics Conference in 2007 and published as Paper AIAA-2007-4299.

References

[1] Smith, A.M.O. “High-Lift Aerodynamics”, 37th Wright Brothers Lecture, AIAA Paper No. 74-939, *AIAA 6th Aircraft Design, Flight Test and Operations Meeting*, Los Angeles, CA, August 12-14, 1974.

[2] Van der Burg, J.W. et al. “Geometrical Model Installation and Deformation Effects in the EUROPEAN Project EUROLIFT II”, *AIAA 25th Applied Aerodynamics Conference*, Miami, FL, June 25-28, 2007 (to be published).

[3] CATIA V5, Release R14, Dassault Systems, http://www.3ds.com

[4] Centaur, Release 6.0.3, CentaurSoft™, http://www.centaursoft.com

[5] Van der Burg, J.W., van der Heul, D., Schippers, H. “Experiences with unstructured grid coarsening for conformal antennas”, *Proceedings of the 9th International Conference on Numerical Grid Generation in Computational Field Simulations*, San Jose, USA, June 2005.

[6] Gerhold, T. “Overview of the Hybrid RANS Code TAU”, *Notes on Numerical Fluid Mechanics and Multidisciplinary Design*, Vol. 89, ISBN 3-540-24383-6, pp. 81-92.

[7] Eliasson, P. “EDGE a Navier-Stokes solver for unstructured grids”, *Proceedings to Finite Volumes for Complex Applications III.*, ISBN 1 9039 9634 1, 2002, pp. 527-534.

[8] Selmin V. and Formaggia, L. “A Unified Approach for the Construction of Finite Element and Finite Volume Discretizaions for Compressible Flow”, *Int. Journal on Numerical Methods in Engineering*, Vol. 34, 1996, pp 1-32.

[9] Cambier, L., Gaziax, M., “elsA : An Efficient Object-Oriented Solution to CFD Complexity”, *40th AIAA Aerospace Science Meeting and Exhibit*, Reno, Nevada, January 14-17, 2002.

[10] ANSYS, ICEM HEXA, http://www.ansys.com

[11] Moen, F. et al. “Transition prediction and impact on 3D high-lift wing configuration” , *AIAA 25th Applied Aerodynamics Conference*, Miami, FL, June 25-28, 2007 (to be published).

[12] Spalart P.R. and Allmaras S.R. “A one-equation turbulence model for aerodynamic flows”, Paper 92-0439, AIAA, 1992.

[13] Hellsten, A. “New Advanced k-w Model for High Lift Aerodynamics”, *AIAA Journal*, Vol. 43, No. 9, pp. 1857-1869,2005

[14] Eliasson, P., “Numerical validation of half model high-lift configuration in a wind tunnel”, *45th AIAA Aerospace Science Meeting and Exhibit*, AIAA-2007-262, Reno, Nevada, USA, January 2007.

[15] Destarac D., “Far-Field / Near Field Drag Balance Application of Drag Extraction in CFD”, *VKI Lecture Series 2003-3*, CFD-Based Aircraft Drag Prediction and Reduction, National Institute of Aerospace, Hampton, VA, November 3-7, 2003.

[16] Selmin, V., Pelizzari, E. and Ghidoni, A. “Fully Anisotropic Unstructured Grid Generation win Application to Aircraft Design”, *proceedings of the ECCOMAS 2006 conference*, P. Wesseling et al eds., TU-Delft, The Netherlands, 2006.